

A Snapshot Survey for Gravitational Lenses Among $z \geq 4.0$ Quasars: II. Constraints on the $4.0 < z < 4.5$ Quasar Population¹

Gordon T. Richards,² Zoltán Haiman,³ Bartosz Pindor,⁴ Michael A. Strauss,² Xiaohui Fan,⁵ Daniel Eisenstein,⁵ Donald P. Schneider,⁶ Neta A. Bahcall,² J. Brinkmann,⁷ and Masataka Fukugita⁸

ABSTRACT

We report on *i*-band snapshot observations of 157 Sloan Digital Sky Survey (SDSS) quasars at $4 < z < 5.4$ using the Advanced Camera for Surveys on the *Hubble Space Telescope (HST)* to search for evidence of gravitational lensing of these sources. None of the quasars appear to be strongly lensed and multiply imaged at the angular resolution ($\sim 0''.1$) and sensitivity of *HST*. The non-detection of strong lensing in these systems constrains the $z = 4$ – 5 luminosity function to an intrinsic slope of $\beta > -3.8$ (3σ), assuming a break in the quasar luminosity function at $M_{1450}^* \sim -24.5$. This constraint is considerably stronger than the limit of $\beta > -4.63$ obtained from the absence of lensing in four $z > 5.7$ quasars. Such constraints are important for our understanding of the true space density of high-redshift quasars and the ionization state of the early universe.

Subject headings: gravitational lensing — early universe — quasars: general — galaxies: luminosity function

²Princeton University Observatory, Peyton Hall, Princeton, NJ 08544.

³Department of Astronomy, Columbia University, 550 West 120th Street, New York, NY 10027.

⁴Department of Astronomy, University of Toronto, 60 St. George Street, Toronto M5S 3H8, Canada.

⁵Steward Observatory, University of Arizona, 933 North Cherry Avenue, Tucson, AZ 85721.

⁶Department of Astronomy and Astrophysics, The Pennsylvania State University, 525 Davey Laboratory, University Park, PA 16802.

⁷Apache Point Observatory, P.O. Box 59, Sunspot, NM 88349.

⁸ICRR/Institute for Cosmic Ray Research, University of Tokyo, 5-1-5 Kashiwa, Kashiwa City, Chiba 277-8582, Japan.

1. Introduction

Investigations of multiply-imaged high-redshift quasars are important for our basic understanding of the formation and growth of supermassive black holes in galactic centers (Turner 1991; Haiman & Loeb 2001) and the ionization state of the universe as a function of time (Madau, Haardt, & Rees 1999; Wyithe & Loeb 2003a). Gravitational lensing changes the apparent flux coming from a quasar and thus changes our interpretation of flux-dependent properties; the discovery that a given quasar is gravitationally lensed means that the naively estimated luminosity is too high. Thus, gravitational lensing would modify the expected size of ionized (H II) regions around individual quasars (Cen & Haiman 2000) and would weaken the lower limits on the neutral fraction in the IGM as inferred from the size of H II regions (Wyithe & Loeb 2004; Mesinger & Haiman 2004). This paper concentrates on the effect that gravitational lensing has on the apparent shape of the quasar luminosity function (Comerford, Haiman, & Schaye 2002; Wyithe & Loeb 2002; Fan et al. 2003). In a previous paper (Richards et al. 2004, hereafter Paper I) we investigated whether the known $z \sim 6$ quasars are gravitationally lensed and discussed how the lack of lenses in this sample affects our understanding of the growth of black holes in the early universe (e.g., Haiman & Loeb 2001) and the ionization history of the universe at the end of the reionization period (e.g., Fan et al. 2002). In this paper, we examine the constraints that can be placed on the intrinsic slope of the quasar luminosity function (QLF) at $z \sim 4\text{--}5$ from a search for gravitational lenses in a sample of $z \sim 4\text{--}5$ quasars (Fan et al. 2001a; Anderson et al. 2001; Schneider et al. 2001; Schneider et al. 2005) in the Sloan Digital Sky Survey (SDSS; York et al. 2000).

Much theoretical effort has been devoted to placing constraints on the slope of the quasar luminosity function from the fraction of lenses found amongst high- z quasars (e.g., Comerford et al. 2002; Wyithe & Loeb 2002). Comerford et al. (2002) showed that modest constraints could be obtained from a sample of ~ 20 $z \sim 6$ quasars from ground-based imaging (i.e., sensitive to $\geq 1''$ splittings), and that similar limits could be derived from *Hubble Space Telescope* (*HST*) resolution imaging of the (then) four known $z \sim 6$ quasars. Paper I presented *HST* imaging showing that none of those four quasars are strongly gravitationally lensed and derived a limit on the slope of the bright end quasar luminosity function of $\beta > -4.63(3\sigma)$. Wyithe (2004) found even stronger constraints for this sample by including the observation that two quasars appear to be lensed by foreground galaxies but are not multiply imaged.

¹Based on observations made with the NASA/ESA Hubble Space Telescope, obtained at the Space Telescope Science Institute, which is operated by the Association of Universities for Research in Astronomy, Inc., under NASA contract NAS 5-26555. These observations are associated with program #9472.

These limits come from magnification bias (Turner, Ostriker, & Gott 1984; Narayan 1989), which would be strong if the slope of the QLF were steep and there were many quasars with intrinsic luminosities below the detection threshold. As discussed in Paper I, the expected fraction of multiply-imaged quasars at a given redshift depends both on the cosmological model and on the luminosity function of quasars. In the WMAP cosmology (Spergel et al. 2003, using a halo distribution taken from the large N-body simulations of Jenkins et al. 2001), the fraction of random lines of sight out to $z = 4$ that produce multiple images at all splitting angles is of order 0.2%; this fraction rises to $\sim 0.4\%$ at $z = 6$. If the intrinsic (unlensed) QLF has a break in slope, then, in general, the fraction of lensed quasars would increase for apparent fluxes above the break. In a flux-limited survey, there is a strong correlation between luminosity and redshift. If the true QLF possesses a break which moves to fainter luminosities at higher redshift, then the most distant quasars (which also look through the longest path length) are expected to be the most likely to be lensed. More explicitly, in the event that no lensing is observed, Paper I showed that the tightest constraints on the QLF slope come from $z \sim 6$ quasars, and also that roughly seven $z \sim 4$ quasars have the same statistical power as a single $z \sim 6$ quasar. Herein we present the results for a sample of 157 $z \sim 4$ quasars from the SDSS that were imaged with *HST*; we find that none of these sources is lensed. As predicted, these quasars provide a constraint on the slope of the QLF that is roughly equivalent to *HST* imaging of 22 $z \sim 6$ quasars, limiting the bright end slope of the $z = 4$ –5 QLF to $\beta > -3.8(3\sigma)$.

Section 2 describes the sample and the data. In § 3 we discuss the constraints on the QLF that can be derived from the data. We summarize in § 4. Throughout this paper, we adopt the WMAP cosmology with $\Omega_m = 0.3$, $\Omega_\Lambda = 0.7$, $H_0 = 70 \text{ km s}^{-1} \text{ Mpc}^{-1}$, an rms mass fluctuation within a sphere of radius $8 h^{-1} \text{ Mpc}$ of $\sigma_8 = 0.9$, and power-law index $n = 0.99$ for the power spectrum of density fluctuations (Spergel et al. 2003). We also adopt the cosmological transfer function from Eisenstein & Hu (1999). Conversions between M_B and M_{1450} assume $M_B = M_{1450} - 0.48$ (Schmidt, Schneider, & Gunn 1995) with spectral index $\alpha_\nu = -0.5$ ($f_\nu \propto \nu^{\alpha_\nu}$).

2. The Data

2.1. Observations and Data Processing

There were 281 SDSS quasars with $z \geq 4.0$ as of January 2002 (Fan et al. 1999, 2000; Zheng et al. 2000; Fan et al. 2001a; Schneider et al. 2001; Anderson et al. 2001), when the sample was defined. Most of these were included in SDSS spectroscopy, but several were discovered as part of early follow-up spectroscopy on the ARC 3.5m telescope and other

telescopes (e.g., Fan et al. 1999), including some that have not yet been published. We were granted the opportunity to observe 250 of these in HST snapshot mode; we did so by including in the sample all quasars with $z \geq 4.6$, and all quasars with $4.0 < z < 4.6$ with $i < 20.3$.

Snapshot observations are carried out with the understanding that not all objects will be observed. In this context, we were able to give objects priorities for being observed. We put the 48 objects with absolute 1450\AA magnitude less than -29 , and/or with $z > 5$ at highest priority, and those with $M_{1450} > -27.95$ at lowest priority. All remaining objects, and those with $4.7 < z < 5$, were placed at medium priority. At the end, 161 objects were observed (of which four were presented in Paper I): 48/48 of the high-priority objects, 97/154 of the medium priority objects, and 16/48 of the low-priority objects.

The four $z > 5.7$ quasars included in our *HST* snapshot program were presented in Paper I. In this paper, we describe the results of imaging of 157 SDSS quasars with $4 < z < 5.4$; see Table 1. For the sake of completeness, we also tabulate those 89 sources that were included in our sample, but were never observed by *HST*, see Table 2. Seven objects in Table 1 and five objects in Table 2 are previously unpublished.

Images of the 157 quasars were acquired with the High Resolution Camera (HRC) on the Advanced Camera for Surveys (ACS). Observations were taken in the SDSS *i*-band (F775W). The Wide-Field Camera on ACS has higher sensitivity in *i* than does the HRC, but has substantially higher overhead and is mildly undersampled. The exposure times were 640 seconds for each object, 320 seconds in each of two exposures to help in cosmic ray rejection.

The data processing was discussed in detail in Paper I, but we briefly review the process here. The raw images were calibrated by the CALACS package in IRAF² as part of on-the-fly-reprocessing (OTFR) at the time of download. The images that we present are the “cosmic ray rejected” (CRJ) images that are output by the OTFR algorithms at STScI. The CRJ files have all been reduced in the standard manner, including having been overscan-, bias- and dark-corrected, flat-fielded and photometrically calibrated, in addition to having bad pixels masked and cosmic rays removed (see the ACS manual³ for more details).

²IRAF is distributed by the National Optical Astronomy Observatories, which are operated by the Association of Universities for Research in Astronomy, Inc., under cooperative agreement with the National Science Foundation.

³<http://www.stsci.edu/hst/acs/documents/handbooks/cycle12/cover.html>

2.2. Subtracting the Point Source and Looking for Multiple Images

HST resolution data are needed for this project as the median expected splitting of gravitationally lensed quasars is predicted (and observed) to be somewhat less than $1''$ (Turner et al. 1984; Hinshaw & Krauss 1987; Browne et al. 2003) and the SDSS images themselves have point-spread-function (PSF) widths of order $1'' - 1''.8$ (Abazajian et al. 2003) with an image scale of $0''.396 \text{ pixel}^{-1}$. Our ACS images, on the other hand, have an image scale of $0''.025 \text{ pixel}^{-1}$ and the point spread function is narrow enough that any lens with a separation greater than $\sim 0''.2$ will be obvious by visual inspection, as we show explicitly in Paper I. These observations should therefore be sensitive to essentially all expected lenses.

We search for faint secondary images at separations smaller than a few tenths of an arcsecond by fitting and removing a model for the point spread function of each image. We use version v6.1 (which includes on-orbit updates for ACS) of the Tiny Tim software (Krist 1995)⁴, which produces a model PSF for the instruments on *HST* given the object’s (observed) spectral energy distribution and position in the focal plane, the filter curve, and knowledge of the optics of the instrument. We fit the PSF model to each CRJ image, allowing the location on the CCD and normalization to vary, and using sinc interpolation when shifting the model PSF by fractional pixels. Example PSF-subtracted images are shown in Figure 1. Each of the images shows the familiar first Airy ring; on a very hard stretch, the second Airy ring is faintly visible.

As discussed in Paper I, for a secondary image offset by $0''.1$ with a flux ratio of 10:1, the secondary object is visible as an enhancement in the first Airy ring of the primary object; it becomes clear upon PSF subtraction (Fig. 1). With a flux ratio of 100:1, we cannot discern a pair with $0''.1$ separation even after subtraction of the PSF; however, even if we were able to do so, it would not significantly improve the constraints that we derive below since most split images will have larger image separations.

None of our 157 targets appears to be gravitationally lensed. Figure 1 shows only the ten objects (both with and without PSF subtraction) which displayed any hint of a second object within the $5''$ field of view. Based on their brightness and morphology, these secondary objects are most likely to be galaxies along the line of sight to the target objects or (in some cases) uncorrected cosmetic defects.

⁴<http://www.stsci.edu/software/tinytim/>

2.3. Accounting for Extended-Source Selection Effects

Since a gravitationally lensed pair of quasars with separation roughly comparable to the seeing size may be classified as extended (rather than point) sources, we must account for the effect that a morphological selection criterion has on our analysis. For the very highest redshift ($z \gtrsim 5$) quasars found from SDSS imaging (e.g., Fan et al. 2001a, and references therein), there is no selection bias against lensed quasars since no morphology restriction was imposed. However, for somewhat lower redshift sources, which were selected with the automated pipeline (Richards et al. 2002), there is a strong bias against high- z ($z \gtrsim 3$) quasars that appear extended (whether due to lensing or errors in morphological classification as a result of low S/N). This bias is intentional; the survey cannot afford the fibers that would be needed to explore all of the extended sources in the high- z quasar portion of the SDSS color-color diagram. The vast majority of these objects are faint moderate-redshift ($0.4 < z < 1$) galaxies.

As discussed in Paper I and Pindor et al. (2003), in order to test the ability of the SDSS photometric pipeline to identify quasar pairs, we created simulated SDSS images of pairs of point sources in these observing conditions and at the appropriate signal-to-noise ratio. The SDSS star-galaxy separator would have classified as a galaxy, and hence excluded from the spectroscopic sample, any pair of point sources having both an image separation $\sim 1'' < \Delta\theta < \sim 2''$, and a flux ratio less than $\sim 5:1$. Thus the SDSS data are suitable for exploring only a fraction of the parameter space of lensing (in terms of separations and flux ratios) that is of interest.

The morphological selection likelihood depends on the luminosity and on the assumed lensing flux ratio and splitting angle, for any given individual quasar. We therefore fold this bias into our probability calculations below on an object-by-object basis. For a given quasar in our sample that has an apparent magnitude of i_s at redshift z_s , and for a given hypothesized magnification factor μ_s (which, for a singular isothermal sphere [SIS], implies a flux ratio of $(\mu_s + 2)/(\mu_s - 2)$) for a lensing halo of mass M (which determines the splitting angle θ_s), we compute the probability $P_s(i_s, z_s, \mu_s, M)$ that the object would have been classified as extended and discarded by the photometric pipeline.

To compute the impact of the selection on our final constraints, we compute the product of the selection likelihood with the expected lensing probability, which gives the probability that this quasar would have been selected by SDSS *and* strongly lensed: $P_{\text{lens}}(z, M) = [1 - P_s(i_s, z_s, \mu_s, M)] \times P_{\text{lens},0}(\mu_s, M)$, where $P_{\text{lens},0}$ is the probability of multiply-imaged lensing in the absence of any other selection effects. Finally, we integrate this product over all combinations of magnifications and lensing halo masses that yield two detectable images with *HST*. We find that typically the inclusion of the morphological selection reduces the

total lensing probability by a factor of three (i.e., the value of the above-defined integral would be three times larger if the factor $P_s(i_s, z_s, \mu_s, M)$ was excluded). More specifically, we find that only $\sim 1/3$ of true lenses would have made it into our sample, with $\sim 2/3$ being classified as extended sources. In Table 1, we list the overall lensing probability for each source. Sixteen of the 157 sources were selected without regard to morphology (as indicated in Table 1); we therefore did not apply the selection function to these objects.

We note that there is a further possible selection effect due to the fact that PSF magnitudes do not contain 100% of the flux from a gravitationally lensed pair of images, hence effectively reducing the magnification bias. This effect turns out to be less significant, partly because those lensed objects for which it would be most important are already removed from the sample by the star-galaxy morphological bias. Overall, we find the effect is likely to shift the luminosity scale by ~ 0.1 magnitudes or less, and we ignore it in what follows.

3. Constraining the Slope of the Quasar Luminosity Function

As discussed in Paper I, existing constraints on the high-redshift QLF are limited by sample size and to the most luminous objects. Schmidt et al. (1995), using a set of 90 quasars with $2.7 < z < 4.8$, found a power-law luminosity function slope (β) of roughly -2 . Fan et al. (2001b) measured $\beta \approx -2.5 \pm 0.3$ from 39 quasars in the redshift interval 3.6 to 5.0. However, this relatively shallow apparent slope does not necessarily represent the intrinsic slope of the QLF, which is expected to be much steeper if a substantial fraction of these quasars are magnified by lensing (e.g., Schneider, Ehlers, & Falco 1992).

In line with Paper I and previous work, we describe the intrinsic (not necessarily observed) quasar luminosity function as a broken power law (e.g., Boyle, Shanks, & Peterson 1988; Pei 1995):

$$\Phi_{\text{int}}(L) = \frac{\Phi_*/L_*}{(L/L_*)^{-\beta_l} + (L/L_*)^{-\beta_h}}. \quad (1)$$

The QLF is described by four parameters: the normalization Φ_* , the faint-end slope β_l , the bright-end slope β_h , and the characteristic luminosity L_* at which the QLF steepens. The lensing probability is most sensitive to the last two parameters, β_h and L_* . The faint end slope has negligible impact on our analysis and we set it to $\beta_l = -1.64$ (e.g., Pei 1995). We apply the lensing model from Comerford et al. (2002), in which lenses are associated with dark matter halos, to compute the total lensing probability, including the effect of magnification bias. In this model, the abundance of halos as a function of potential well depth is adopted from the simulations of Jenkins et al. (2001). As discussed in Paper I, we assume that all halos below $M \approx 10^{13} M_\odot$ have SIS profiles (adopting a standard conversion

between circular velocity and halo mass), while all halos above this mass follow the dark matter density profile suggested by Navarro, Frenk, & White (1997, hereafter NFW). NFW profiles are much less efficient lenses than are SIS profiles. This prescription is essentially equivalent to ignoring all lenses above a halo mass of $10^{13}M_{\odot}$, as the massive halos do not contribute to lensing at small separations. We do not include here more complex lens models, such as those including external shear or ellipticity. As discussed by Keeton, Kuhlen, & Haiman (2005), such models can, in general, boost the lensing probabilities (although that paper considered in detail only the boost that can occur for singly-imaged lensing probabilities).

In the case of $\beta_h = -3.8$ and $M_{1450}^* = -24.52$, the mean probability for lensing is about 4% for each source. The morphology selection effect causes this mean probability to be reduced by about a factor of 3 (as discussed above). In Table 1 we list each of the quasars that were observed by *HST* and list their lensing probabilities, which vary relatively little from source to source. The median redshift of the sample is $z = 4.35$.

The lack of lenses among these 157 quasars allows us to place constraints on the QLF at high redshift, shown in Figure 2. The lensing probability is a function of both the break and the faint-end slope. Assuming a break of $M_B^* = -25.0$ ($M_{1450}^* = -24.52$), the above lensing probabilities yield a $3\text{-}\sigma$ constraint on the bright end slope of $\beta > -3.8$.⁵ Note that we have used a somewhat brighter break luminosity than we did in Paper I for the $z \sim 6$ quasars as the characteristic luminosity is thought to evolve with redshift. Since this choice of break luminosity is somewhat arbitrary (as it is an extrapolation from low-redshift and the QLF may not even exhibit a strong break at high- z), we also show the constraints on β as a function of break luminosity in Figure 2.

Finally, it is useful to consider constraints that we can place on the underlying lensing halo population. Without any magnification bias, the total optical depth to multiply-imaged lensing at $z \sim 4.5$ is only 0.25 percent, which is reduced by the SDSS morphological selection to 0.08 percent. This makes the lack of lenses among our 157 sources unsurprising. We find that to reduce the probability of not finding even one lens in the whole sample, the single-object lensing probability must be boosted by a factor of about 40 (this is essentially the typical magnification bias produced by the model QLF we constrain at 3σ). As a result, we rule out (at 3σ confidence) lensing models in which there are $\gtrsim 40$ times more galaxies than implied by the halo mass function we adopted from Jenkins et al. While this is a weak constraint, it is still the best direct limit on the number density of $M \sim 10^{12} M_{\odot}$ halos at

⁵This constraint weakens if the intrinsic bright end slope steepens with luminosity instead of being a single power law.

$1 < z < 2$ (the redshift and mass range dominating the expected lensing probability; see Figure 1 in Comerford et al. 2002).

4. Discussion and Conclusions

Constraining the high- z QLF slope is particularly important to understand the roles of accretion and feedback in the growth of galaxies (e.g., Silk & Rees 1998; Fabian 1999; Wyithe & Loeb 2003b; Hopkins et al. 2005a). For the most luminous quasars with $z \lesssim 2.5$ (i.e., the redshift at which the quasar comoving density peaks), the bright end slope has been shown to be $\beta \sim -3.3$ (Croom et al. 2004; Richards et al. 2005). For the most luminous quasars at $z > 4$, the measured slope is $\beta \sim -2.5$ (Fan et al. 2001a). While the slope of the QLF has been well measured, understanding the physical processes behind the QLF and its evolution are still open questions and various explanations have been proposed. Wyithe & Loeb (2003a) suggest that feedback mechanisms may prevent the gas in the most massive dark matter halos from collapsing at low- z , suppressing the number of luminous low- z quasars relative to high- z . Alternatively, in the model of Hopkins et al. (2005a, 2005b), the bright end of the QLF is defined by near-Eddington accretion at the peak luminosity in the history of a quasar, whereas the faint end slope may be due to sub-Eddington accretion. Tighter limits on the bright end slope of the high-redshift QLF provide important constraints that any such models must account for.

In this work, we have obtained high resolution *HST* images of 157 $4 < z < 5.4$ redshift quasars (known prior to September 2001) to look for the signature of gravitational lensing. We have found no evidence of multiple images, significantly limiting the amount by which these quasars can be magnified by foreground mass concentrations (in the absence of microlensing). The lack of any strong lenses puts a 3σ constraint on the intrinsic bright end slope of the $z = 4-5$ luminosity function of $\beta_h > -3.8$. Our sample has a strong bias against pairs with $\theta > 1''$ due to the exclusion of objects which appear extended in SDSS images. We are currently exploring methods for cleanly selecting such wide separation pairs from the SDSS imaging data.

Funding for the creation and distribution of the SDSS Archive has been provided by the Alfred P. Sloan Foundation, the Participating Institutions, the National Aeronautics and Space Administration, the National Science Foundation, the U.S. Department of Energy, the Japanese Monbukagakusho, and the Max Planck Society. The SDSS Web site is <http://www.sdss.org/>. The SDSS is managed by the Astrophysical Research Consortium (ARC) for the Participating Institutions. The Participating Institutions are The University

of Chicago, Fermilab, the Institute for Advanced Study, the Japan Participation Group, The Johns Hopkins University, the Korean Scientist Group, Los Alamos National Laboratory, the Max-Planck-Institute for Astronomy (MPIA), the Max-Planck-Institute for Astrophysics (MPA), New Mexico State University, University of Pittsburgh, University of Portsmouth, Princeton University, the United States Naval Observatory, and the University of Washington. Support for program #9472 was provided by NASA through a grant (HST-GO-09472.01-A; M. A. S and G. T. R.) from the Space Telescope Science Institute, which is operated by the Association of Universities for Research in Astronomy, Inc., under NASA contract NAS 5-26555. This work was supported in part by NASA ATP grant NNG04GI88G (Z. H.), National Science Foundation grants AST-0307582 (D. P. S.), AST-0307409 (M. A. S.), AST-0307384 (X. F.), AST-0307291 (Z. H.) and AST-0307200 (Z. H.). X. F. and D. J. E. acknowledge Alfred P. Sloan Research Fellowships. X. F. further acknowledges support from a David and Lucile Packard Fellow in Science and Engineering.

REFERENCES

- Abazajian, K., Adelman-McCarthy, J. K., Agüeros, M. A., Allam, S. S., Anderson, S. F., Annis, J., Bahcall, N. A., Baldry, I. K., et al. 2003, *AJ*, 126, 2081
- Anderson, S. F., Fan, X., Richards, G. T., Schneider, D. P., Strauss, M. A., Vanden Berk, D. E., Gunn, J. E., Knapp, G. R., et al. 2001, *AJ*, 122, 503
- Boyle, B. J., Shanks, T., & Peterson, B. A. 1988, *MNRAS*, 235, 935
- Browne, I. W. A., Wilkinson, P. N., Jackson, N. J. F., Myers, S. T., Fassnacht, C. D., Koopmans, L. V. E., Marlow, D. R., Norbury, M., et al. 2003, *MNRAS*, 341, 13
- Cen, R. & Haiman, Z. 2000, *ApJ*, 542, L75
- Comerford, J. M., Haiman, Z., & Schaye, J. 2002, *ApJ*, 580, 63
- Croom, S. M., Smith, R. J., Boyle, B. J., Shanks, T., Miller, L., Outram, P. J., & Loaring, N. S. 2004, *MNRAS*, 349, 1397
- Eisenstein, D. J. & Hu, W. 1999, *ApJ*, 511, 5
- Fabian, A. C. 1999, *MNRAS*, 308, L39
- Fan, X., Narayanan, V. K., Strauss, M. A., White, R. L., Becker, R. H., Pentericci, L., & Rix, H. 2002, *AJ*, 123, 1247

- Fan, X., Strauss, M. A., Richards, G. T., Newman, J. A., Becker, R. H., Schneider, D. P., Gunn, J. E., Davis, M., et al. 2001a, *AJ*, 121, 31
- Fan, X., Strauss, M. A., Schneider, D. P., Becker, R. H., White, R. L., Haiman, Z., Gregg, M., Pentericci, L., et al. 2003, *AJ*, 125, 1649
- Fan, X., Strauss, M. A., Schneider, D. P., Gunn, J. E., Lupton, R. H., Anderson, S. F., Voges, W., Margon, B., et al. 2000, *AJ*, 119, 1
- Fan, X., Strauss, M. A., Schneider, D. P., Gunn, J. E., Lupton, R. H., Becker, R. H., Davis, M., Newman, J. A., et al. 2001b, *AJ*, 121, 54
- Fan, X., Strauss, M. A., Schneider, D. P., Gunn, J. E., Lupton, R. H., Yanny, B., Anderson, S. F., Anderson, J. E., et al. 1999, *AJ*, 118, 1
- Haiman, Z. & Loeb, A. 2001, *ApJ*, 552, 459
- Hinshaw, G. & Krauss, L. M. 1987, *ApJ*, 320, 468
- Hopkins et al. 2005a, [astro-ph/0504252](#)
- . 2005b, [astro-ph/0504253](#)
- Jenkins, A., Frenk, C. S., White, S. D. M., Colberg, J. M., Cole, S., Evrard, A. E., Couchman, H. M. P., & Yoshida, N. 2001, *MNRAS*, 321, 372
- Keeton, C. R., Kuhlen, M., & Haiman, Z. 2005, *ApJ*, 621, 559
- Krist, J. 1995, in *ASP Conf. Ser. 77: Astronomical Data Analysis Software and Systems IV*, 349
- Madau, P., Haardt, F., & Rees, M. J. 1999, *ApJ*, 514, 648
- Mesinger, A. & Haiman, Z. 2004, *ApJ*, 611, L69
- Narayan, R. 1989, *ApJ*, 339, L53
- Navarro, J. F., Frenk, C. S., & White, S. D. M. 1997, *ApJ*, 490, 493
- Pei, Y. C. 1995, *ApJ*, 438, 623
- Pindor, B., Turner, E. L., Lupton, R. H., & Brinkmann, J. 2003, *AJ*, 125, 2325
- Richards, G. T., Croom, S. M., Anderson, S. F., Bland-Hawthorn, J., Boyle, B. J., De Propris, R., Drinkwater, M. J., Fan, X., et al. 2005, *MNRAS*, 360, 839

- Richards, G. T., Fan, X., Newberg, H. J., Strauss, M. A., Vanden Berk, D. E., Schneider, D. P., Yanny, B., Boucher, A., et al. 2002, *AJ*, 123, 2945
- Richards, G. T., Strauss, M. A., Pindor, B., Haiman, Z., Fan, X., Eisenstein, D., Schneider, D. P., Bahcall, N. A., et al. 2004, *AJ*, 127, 1305 (PaperI)
- Schmidt, M., Schneider, D. P., & Gunn, J. E. 1995, *AJ*, 110, 68
- Schneider, D. P., Fan, X., Strauss, M. A., Gunn, J. E., Richards, G. T., Hill, G. J., MacQueen, P. J., Ramsey, L. W., et al. 2001, *AJ*, 121, 1232
- Schneider, D. P., Hall, P. B., Richards, G. T., Vanden Berk, D. E., Anderson, S. F., Fan, X., Jester, S., Stoughton, C., et al. 2005, *AJ*, 130, 367
- Schneider, P., Ehlers, J., & Falco, E. E. 1992, *Gravitational Lenses* (Springer-Verlag Berlin)
- Silk, J. & Rees, M. J. 1998, *A&A*, 331, L1
- Spergel, D. N., Verde, L., Peiris, H. V., Komatsu, E., Nolta, M. R., Bennett, C. L., Halpern, M., Hinshaw, G., et al. 2003, *ApJS*, 148, 175
- Turner, E. L. 1991, *AJ*, 101, 5
- Turner, E. L., Ostriker, J. P., & Gott, J. R. 1984, *ApJ*, 284, 1
- Wyithe, J. S. B. 2004, *MNRAS*, 351, 1266
- Wyithe, J. S. B. & Loeb, A. 2002, *ApJ*, 577, 57
- . 2003a, *ApJ*, 586, 693
- . 2003b, *ApJ*, 595, 614
- . 2004, *Nature*, 432, 194
- York, D. G., Adelman, J., Anderson, J. E., Anderson, S. F., Annis, J., Bahcall, N. A., Bakken, J. A., Barkhouser, R., et al. 2000, *AJ*, 120, 1579
- Zheng, W., Tsvetanov, Z. I., Schneider, D. P., Fan, X., Becker, R. H., Davis, M., White, R. L., Strauss, M. A., et al. 2000, *AJ*, 120, 1607

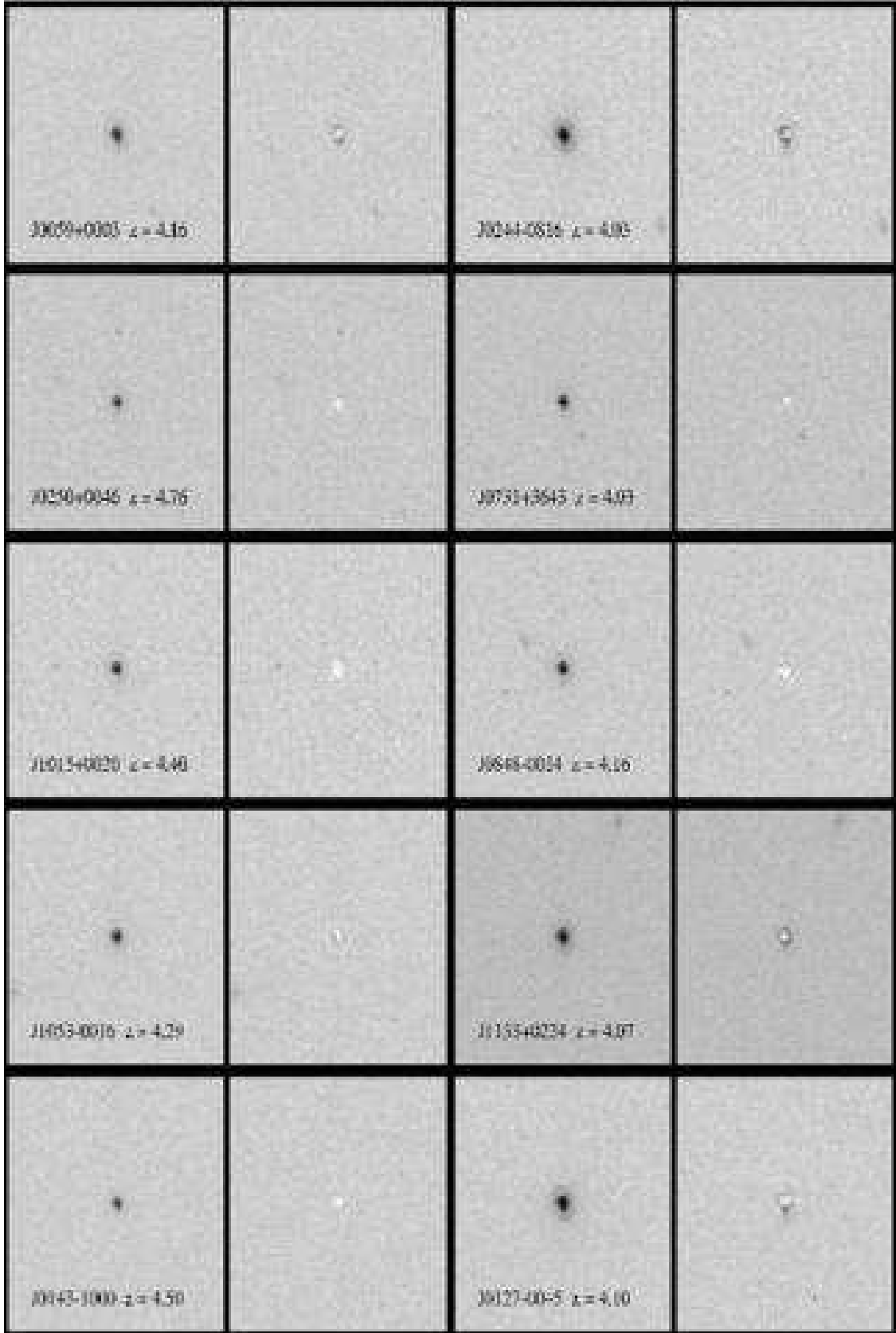


Fig. 1.— *HST*/ACS/HRC F775W images of the 10 high- z SDSS quasars that show any sign of a secondary object in a $5''$ field of view. The scale is $5'' \times 5''$ in each of the panels. The left hand panel is the “cosmic ray rejected” (CRI) output of GALAXY. The right hand panel is

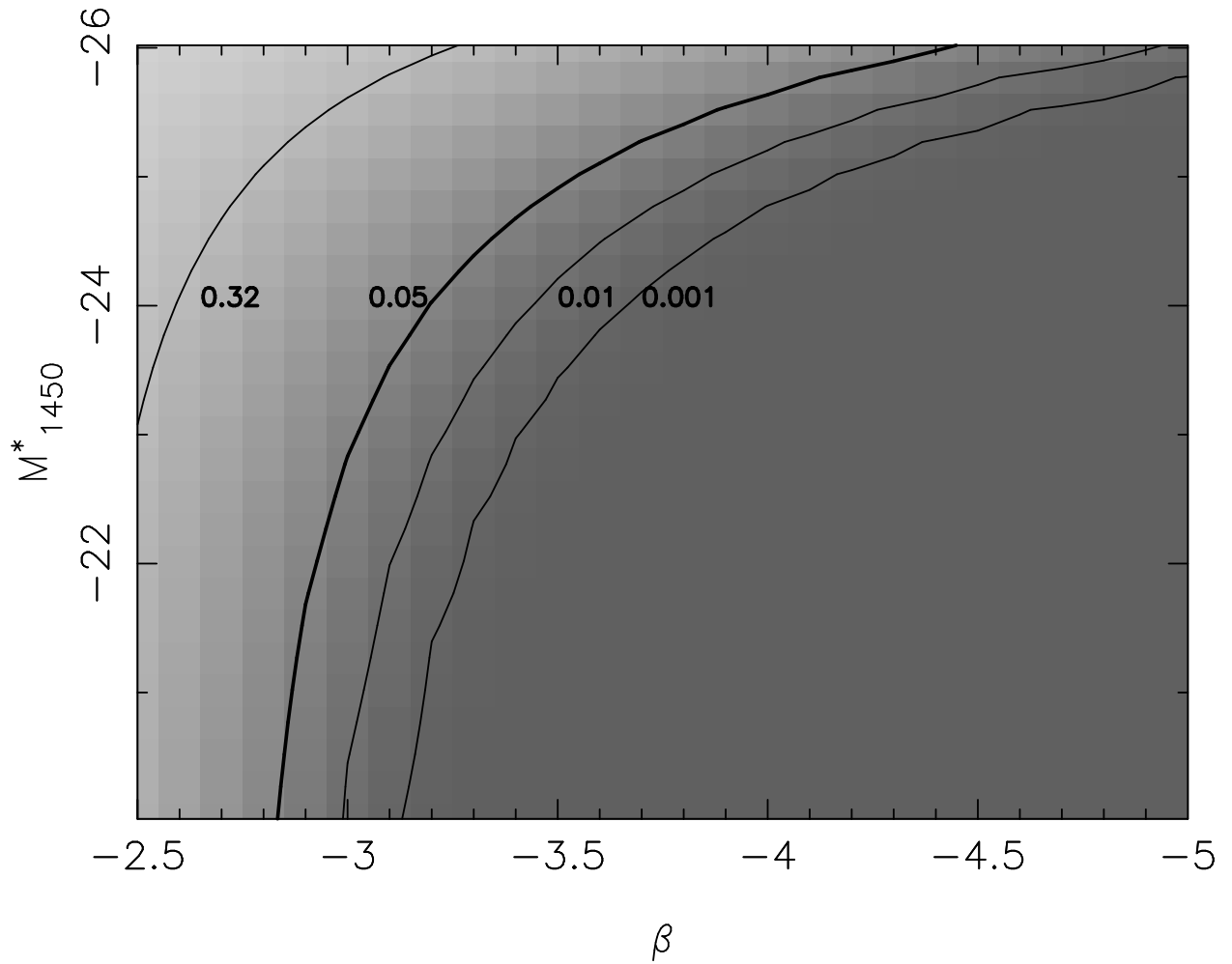


Fig. 2.— Contours of fixed likelihood for no lensing among the 157 $z \sim 4.35$ quasars, shown in the two-dimensional parameter space of the slope and break of the $z \sim 4.35$ quasar luminosity function. The 3σ limit on β given an assumed break in the luminosity function of $M_{1450}^* = -24.5$ is $\beta = -3.8$.

Table 1.

SDSS J	Redshift	M_B	SDSS i	HST i	$P_{\text{lens},0}$	P_{lens}	HST ID	Ref
001115.23+144601.8	4.924	−28.39	18.41	18.26	0.3137	0.0906	aa	7
001134.52+155137.3	4.394	−26.20	20.20	19.91	0.0553	0.0164	ab	7
001714.66−100055.4	4.976	−26.85	19.61	19.46	0.1103	0.0277	ac	7
001813.88+142455.6	4.221	−26.81	19.41	19.30	0.0945	0.0269	ad	7
001918.43+150611.3	4.134	−26.27	19.91	19.94	0.0563	0.0160	ae	7
001950.06−004040.7	4.352	−26.65	19.50	19.36	0.0842	0.0345	af	3
002618.67+140946.7	4.578	−26.64	20.11	19.68	0.0868	0.0221	ag	7
003525.28+004002.7*	4.750	−26.77	19.42	19.90	0.0999	0.0999	ai	1
003618.84−004629.9	4.040	−26.46	19.89	19.57	0.0662	0.0175	aj	0
003714.11−005603.9*	4.350	−26.49	20.27	20.55	0.0727	0.0727	ak	6
003749.19+155208.4	4.076	−26.05	19.72	19.72	0.0443	0.0182	al	6
004054.65−091526.8	4.972	−27.73	19.35	19.05	0.2124	0.0531	am	7
005006.35−005319.2	4.416	−26.95	19.53	19.39	0.1104	0.0303	an	6
005922.65+000301.4	4.161	−26.97	19.43	19.24	0.1069	0.0394	ao	3
010619.25+004823.4	4.430	−27.73	18.70	18.59	0.1980	0.0546	aq	6
012004.82+141108.2	4.720	−25.78	20.22	20.45	0.0375	0.0120	ar	6
012019.99+000735.5	4.085	−26.31	19.82	19.87	0.0579	0.0230	as	3
012211.11+150914.3	4.510	−27.60	18.67	18.65	0.1835	0.0574	at	7
012405.70−004407.8	4.008	−26.57	19.56	19.42	0.0728	0.0200	au	7
012700.69−004559.2	4.103	−27.91	18.30	18.11	0.2105	0.0668	av	3
013242.76−094301.6	4.268	−26.62	19.71	19.53	0.0807	0.0211	aw	7
014328.37−100019.3	4.496	−26.36	20.10	20.16	0.0660	0.0190	ax	7
014609.33−092918.2	4.153	−26.32	19.92	19.73	0.0593	0.0168	ay	7
015339.60−001104.8	4.205	−27.23	18.74	18.81	0.1329	0.0399	a0	6
015704.10+122858.2	4.191	−26.06	19.90	19.90	0.0460	0.0151	a1	6
020326.46−003954.0	4.169	−27.02	19.45	19.15	0.1116	0.0315	a3	0
020651.37+121624.3*	4.810	−26.79	19.89	19.84	0.1025	0.1025	a4	6
021043.15−001818.2	4.697	−27.11	19.54	19.14	0.1313	0.0406	a5	3
021102.72−000910.2*	4.900	−27.05	19.93	20.04	0.1286	0.1286	a6	1
023137.65−072854.5	5.410	−69.14	19.53	19.55	0.0073	0.0029	a8	6
023923.47−081005.1	4.019	−26.46	19.27	19.18	0.0658	0.0204	a9	6
024447.78−081606.1	4.030	−28.03	18.03	18.19	0.2240	0.0785	ba	6
024457.19−010809.8	4.010	−26.46	18.33	18.26	0.0657	0.0266	bb	3
025019.78+004650.3*	4.760	−27.03	19.65	19.72	0.1243	0.1243	bc	3
025647.06−085041.3	4.228	−26.95	19.62	19.65	0.1066	0.0308	bf	6
030025.22+003224.3	4.188	−26.12	20.18	19.90	0.0489	0.0192	bg	3
031213.97−062658.8	4.030	−27.12	19.08	19.08	0.1174	0.0341	bj	6
032608.12−003340.1	4.175	−26.89	19.26	19.51	0.1003	0.0279	bl	1
033119.66−074143.1	4.700	−27.21	19.10	19.35	0.1420	0.0393	bm	6
033305.32−053708.9	4.270	−26.07	19.79	19.83	0.0473	0.0172	bn	6
033829.31+002156.2	5.001	−26.29	20.15	19.96	0.0668	0.0199	bo	1
035214.33−001941.0*	4.180	−26.46	19.76	19.78	0.0683	0.0683	bs	3
040550.26+005931.1*	4.050	−25.85	20.07	20.07	0.0356	0.0356	bt	3
043225.11−005625.9*	4.020	−25.47	19.77	19.89	0.0230	0.0230	bu	0
073147.00+364346.5	4.030	−27.12	19.29	19.22	0.1174	0.0369	bv	6
074640.16+344624.7	4.032	−26.73	19.34	19.31	0.0846	0.0259	bx	7

Table 1—Continued

SDSS J	Redshift	M_B	SDSS i	HST i	$P_{\text{lens},0}$	P_{lens}	HST ID	Ref
075103.95+424211.5	4.160	−27.35	18.82	18.87	0.1443	0.0450	bz	6
075618.14+410408.5	5.090	−26.60	20.21	20.07	0.0915	0.0234	b0	6
075652.07+450258.9	4.812	−26.37	20.24	20.23	0.0700	0.0199	b1	6
075732.90+441424.6	4.179	−26.94	19.38	19.42	0.1047	0.0300	b2	6
081054.88+460357.8	4.087	−27.46	18.38	18.53	0.1542	0.0478	b5	6
083100.68+434426.9	4.452	−26.42	20.08	19.95	0.0694	0.0188	b7	7
083103.00+523533.5	4.512	−27.00	19.37	19.28	0.1169	0.0329	b8	6
083212.38+530327.4	4.081	−26.74	19.46	19.28	0.0863	0.0258	b9	6
083941.45+031817.0	4.244	−27.61	18.79	18.55	0.1769	0.0543	cc	7
083946.21+511202.8	4.415	−27.71	18.98	18.83	0.1949	0.0597	cd	6
084811.52−001417.9	4.156	−27.38	18.99	18.93	0.1474	0.0456	ce	6
085151.26+020756.0	4.294	−26.75	19.41	19.27	0.0910	0.0250	cf	6
085210.89+535948.9	4.275	−26.45	19.82	19.77	0.0690	0.0189	cg	6
085227.28+504510.8	4.219	−27.70	18.82	18.63	0.1873	0.0546	ch	7
090100.61+472536.1	4.610	−26.70	19.76	19.56	0.0920	0.0275	ck	7
090440.63+535038.8	4.298	−27.27	19.25	19.48	0.1394	0.0393	cm	6
090634.84+023433.8	4.544	−27.71	18.77	18.66	0.1987	0.0712	co	7
091316.55+591921.4	5.110	−26.38	20.50	20.47	0.0751	0.0179	cq	6
092038.49+564235.9	4.183	−26.62	19.95	19.06	0.0793	0.0239	cr	6
092256.19+561849.1	4.198	−27.19	18.99	19.67	0.1286	0.0403	cs	6
093931.90+003955.0*	4.500	−26.74	20.62	20.29	0.0936	0.0936	cv	5
094056.02+584830.1	4.660	−27.06	19.27	19.41	0.1255	0.0361	cw	6
094108.35+594725.8	4.820	−27.10	19.36	19.25	0.1325	0.0369	cx	6
094917.18+602104.4	4.290	−26.01	20.26	20.20	0.0446	0.0136	cy	6
095151.17+594556.2	4.860	−26.41	19.81	19.73	0.0732	0.0218	c0	6
095511.33+594030.7	4.356	−27.68	18.30	18.56	0.1892	0.0552	c1	7
101053.52+644832.1	4.745	−26.35	19.87	19.98	0.0680	0.0182	c3	6
101549.00+002019.9	4.399	−27.02	19.27	19.23	0.1166	0.0336	c4	6
102043.82+000105.7	4.160	−26.08	19.83	19.88	0.0466	0.0182	c5	6
102119.16−030937.1*	4.696	−25.88	20.08	20.29	0.0417	0.0417	c6	4
102332.08+633508.1	4.880	−27.00	19.69	19.44	0.1232	0.0342	c7	6
103432.72−002702.5	4.380	−26.17	19.90	20.05	0.0535	0.0150	c9	7
104008.10+651429.2	4.583	−26.22	19.83	19.83	0.0584	0.0183	da	6
104040.14−001540.8	4.320	−27.40	18.80	18.94	0.1543	0.0532	db	6
104351.19+650647.6	4.542	−27.15	19.09	18.89	0.1324	0.0371	dc	6
105320.43−001649.5	4.291	−27.01	19.33	19.30	0.1134	0.0343	dg	2
105902.73+010404.1	4.060	−26.89	19.21	19.32	0.0978	0.0292	di	6
110247.29+663519.5	4.810	−26.12	20.47	20.57	0.0546	0.0142	dj	6
110813.86−005944.5	4.029	−26.73	19.25	19.41	0.0845	0.0243	dk	5
110826.31+003706.7	4.502	−26.79	19.84	19.55	0.0978	0.0348	dm	6
111224.18+004630.3	4.032	−26.34	19.66	19.62	0.0588	0.0172	dn	6
111401.47−005321.0	4.590	−26.70	19.57	19.70	0.0917	0.0271	do	2
112242.99−022905.1*	4.795	−26.40	20.38	20.43	0.0719	0.0719	dp	4
112253.51+005329.7	4.570	−26.80	19.12	19.28	0.0998	0.0409	dq	2
112311.13−004418.5*	5.000	−26.28	20.46	20.20	0.0661	0.0661	dr	0
113354.89+022420.9	4.066	−27.41	18.84	18.88	0.1480	0.0444	dt	7

Table 1—Continued

SDSS J	Redshift	M_B	SDSS i	HST i	$P_{\text{lens},0}$	P_{lens}	HST ID	Ref
113559.93+002422.7	4.040	−26.31	19.87	19.64	0.0572	0.0163	du	5
115547.83+022716.1	4.355	−26.81	19.51	19.29	0.0970	0.0273	dx	7
120439.42+663549.7	4.052	−26.72	19.66	19.62	0.0842	0.0252	dy	7
120441.73−002149.6	5.030	−27.19	19.28	19.28	0.1471	0.0646	dz	2
120823.81+001027.6*	5.280	−26.82	20.79	20.59	0.1164	0.1164	d1	1
121422.02+665707.5	4.680	−26.47	18.91	18.96	0.0755	0.0238	d2	7
122600.68+005923.5	4.264	−27.24	18.90	18.83	0.1354	0.0524	d3	2
122622.03+662017.9	4.017	−26.24	20.07	20.05	0.0531	0.0192	d4	7
122657.97+000938.4	4.140	−27.03	19.24	19.31	0.1118	0.0356	d5	7
123503.02−000331.6	4.700	−25.98	20.07	20.04	0.0465	0.0134	d8	2
125759.21−011130.2	4.150	−27.79	18.55	18.40	0.1964	0.0613	ec	6
125847.62−025456.1	4.031	−26.68	19.57	19.45	0.0000	0.0000	ee	7
130002.16+011823.0	4.614	−27.25	18.82	18.73	0.1446	0.1446	ef	7
130619.38+023658.9	4.874	−26.92	19.66	19.61	0.1153	0.0298	ej	7
131052.51−005533.3	4.150	−27.32	18.83	18.85	0.1408	0.0451	ek	2
131831.83+653929.4	4.286	−26.09	20.07	20.17	0.0484	0.0180	el	7
132110.82+003821.6	4.700	−26.46	20.04	20.22	0.0750	0.0255	em	2
134134.19+014157.7	4.725	−27.51	18.93	18.98	0.1776	0.0513	eq	7
134723.08+002158.8	4.270	−27.54	18.96	18.71	0.1692	0.0499	er	6
140146.52+024434.6	4.455	−27.72	18.58	18.53	0.1974	0.0574	ev	7
140248.07+014634.1	4.206	−27.96	18.26	18.12	0.2215	0.0612	ew	7
141306.09+644149.0	4.255	−26.28	19.49	19.34	0.0583	0.0170	ey	7
141315.36+000032.4	4.071	−26.34	19.73	19.54	0.0594	0.0191	ez	2
142911.84+632344.9	4.431	−26.57	20.33	20.33	0.0795	0.0182	e4	7
143352.21+022714.0	4.749	−28.03	18.33	18.32	0.2502	0.0763	e5	7
144255.56+590949.9	4.333	−26.23	20.19	20.04	0.0564	0.0198	e8	7
144340.71+585653.3	4.242	−28.44	18.02	18.09	0.2966	0.0864	e9	7
144413.26+004836.7*	4.780	−26.08	21.00	21.08	0.0522	0.0522	fb	0
144617.35−010131.1	4.185	−27.21	19.09	19.06	0.1303	0.0376	fd	6
144717.97+040112.4	4.508	−27.48	19.33	19.21	0.1686	0.0449	fe	7
145107.94+025615.6	4.486	−27.05	19.11	19.08	0.1212	0.0354	ff	7
145229.37+595156.3	4.029	−26.85	19.54	19.32	0.0938	0.0317	fi	7
145350.38+610109.0	4.134	−26.59	19.50	19.49	0.0763	0.0235	fj	7
145747.66+575332.1	4.355	−26.47	20.04	19.93	0.0714	0.0230	fk	7
150527.34+573632.0	4.385	−26.36	19.98	19.75	0.0647	0.0197	fl	7
150847.60+571501.3	4.876	−26.53	20.06	19.99	0.0821	0.0240	fm	7
151002.92+570243.3	4.310	−26.43	20.06	19.95	0.0682	0.0201	fn	7
151155.98+040802.9	4.621	−26.63	19.85	19.71	0.0866	0.0321	fp	7
161616.25+513336.9	4.528	−26.98	19.58	19.54	0.1153	0.0329	fz	7
163257.07+441110.2	4.105	−27.35	18.93	18.54	0.1427	0.0431	f1	7
163950.51+434003.7	4.007	−28.37	17.91	17.79	0.2738	0.0860	f2	7
165354.62+405402.2	4.966	−27.23	18.79	18.54	0.1491	0.0481	f3	7
170804.89+602201.9	4.350	−26.54	19.78	19.99	0.0762	0.0225	f4	6
171014.51+592326.4	4.536	−26.75	19.67	19.73	0.0950	0.0288	f5	6
171224.92+560624.9	4.229	−26.23	20.02	20.07	0.0552	0.0195	f6	6
171808.67+551511.2	4.620	−26.35	19.99	20.06	0.0667	0.0201	f7	6

Table 1—Continued

SDSS J	Redshift	M_B	SDSS i	HST i	$P_{\text{lens},0}$	P_{lens}	HST ID	Ref
172007.20+602823.8	4.400	−26.20	20.20	20.08	0.0554	0.0188	f8	6
173744.87+582829.5	4.940	−27.35	19.33	19.29	0.1626	0.0476	f9	6
204421.51−052521.9	4.224	−26.88	19.71	19.52	0.1004	0.0232	ga	7
210155.45−062711.8	4.341	−26.09	20.20	19.95	0.0490	0.0130	gb	7
210216.52+104906.5	4.175	−27.34	19.22	18.96	0.1436	0.0470	gc	7
220008.66+001744.8	4.791	−26.93	19.30	19.19	0.1150	0.0324	gg	6
220307.39−004612.0	4.160	−27.11	19.41	18.99	0.1198	0.0506	gh	7
221644.01+001348.2*	4.990	−27.42	20.30	20.31	0.1726	0.1726	gj	6
221855.11+134708.6	4.277	−26.60	19.83	19.53	0.0793	0.0219	gl	7
222509.17−001406.9	4.861	−27.32	19.31	19.07	0.1576	0.0602	gn	7
222845.14−075755.2	5.151	−27.33	20.16	19.83	0.1684	0.0576	gp	7
224243.03−091543.9	4.223	−26.27	19.95	19.88	0.0574	0.0156	gr	7
224630.86+131706.7	4.116	−26.72	19.70	19.65	0.0854	0.0223	gs	7
225843.27−092710.6	4.041	−26.88	19.35	18.95	0.0965	0.0277	gw	7
234003.50+140257.2	4.535	−27.36	19.12	18.91	0.1552	0.0467	g1	7
234025.97+135009.1	4.173	−25.93	20.18	19.93	0.0399	0.0111	g2	7
234750.31+134102.7	4.265	−26.05	19.75	19.63	0.0462	0.0152	g3	7
235152.80+160048.9	4.668	−26.31	19.79	19.83	0.0647	0.0189	g4	7
235344.26+143525.2	4.257	−26.58	19.87	19.66	0.0776	0.0206	g5	7

Note. — Column 1 gives the IAU name of the object (N.B. that SDSS image reprocessing can change the coordinates [by $\sim 0''.1$] and thus the name slightly; matching should thus be done on coordinates, not names). Starred objects were selected without reference to their morphological type (stellar vs. extended). Column 2 is the redshift. Column 3 is the absolute B magnitude, computed with the parameters given in § 1. Columns 4 and 5 give the SDSS and HST i -band magnitudes (uncorrected for Galactic reddening). Column 6 indicates the lensing probability for this object, ignoring morphological selection effects. Column 7 gives the lensing probability after accounting for morphological selection effects. Column 8 give the two character “observation set id” related to the *HST* file naming convention. This is given to facilitate archival use of these data. The program id for this project was “8f3”, thus the files for the first object have names like j8f3aa011_crj.fits. Column 9 gives the discovery reference, which are (1) Fan et al. (1999), (2) Fan et al. (2000), (3) Fan et al. (2001a), (4) Zheng et al. (2000), (5) Schneider et al. (2001), (6) Anderson et al. (2001), and (7) Schneider et al. (2005). A zero in this column means that the objects are being published here for the first time.

Table 2.

SDSS J	Redshift	SDSS <i>i</i>	Ref	SDSS J	Redshift	SDSS <i>i</i>	Ref
003126.80+150739.6	4.291	19.97	7	132853.65–022441.6	4.620	19.91	7
010326.89+005538.6	4.159	20.07	0	133211.90+031556.3	4.727	19.29	7
015032.87+143425.5	4.284	20.09	6	135057.86–004355.3	4.427	19.91	6
020152.53–094733.4	4.026	20.29	7	135134.46–003652.1	4.034	19.88	6
021419.42–010716.9	4.592	20.53	0	135422.99–003906.1	4.420	20.15	6
025039.17–065405.1	4.505	19.84	6	140404.63+031403.9	4.969	19.53	7
025204.28+003136.9	4.119	19.91	6	141332.35–004909.6	4.213	19.30	2
030437.21+004653.6	4.281	20.12	0	141534.91+033132.1	4.451	19.89	7
031036.96–001457.0*	4.630	19.89	1	142004.11+022708.7	4.187	20.09	7
032459.10–005705.1*	4.800	20.69	3	142408.34+024219.9	4.342	19.79	7
034109.35–064805.0	4.142	20.20	6	144117.46+035910.5	4.312	19.60	7
034541.51–072315.3	4.062	19.52	6	144231.72+011055.3	4.560	19.93	6
034946.61–065730.2	4.041	20.23	6	144407.63–010152.7	4.552	19.29	6
073354.93+321241.5	4.446	20.38	7	144428.67–012344.0	4.160	19.47	2
074907.57+355543.8	4.257	20.09	7	145118.77–010446.1*	4.660	20.70	1
080159.24+433624.9	4.166	20.26	6	145212.86+023526.4	4.916	19.92	7
080549.94+482345.8	4.208	19.86	6	151041.79+031810.5	4.230	19.63	7
081241.12+442129.0	4.334	20.21	6	151909.09+030633.7	4.391	19.47	7
083824.32+460443.7	4.011	19.60	7	152245.19+024543.8	4.087	18.91	7
085430.19+004213.6	4.079	20.02	6	152443.19+011358.9*	4.114	19.98	6
085634.93+525206.3	4.790	20.31	6	152740.50–010602.5	4.410	19.95	2
090242.09–002125.8	4.450	19.77	6	152743.86+035301.3	4.226	19.86	7
090532.14–001430.4	4.254	19.89	6	153259.95–003944.0*	4.620	19.73	2
091016.79+575331.0	4.005	19.50	6	160207.95+523717.9	4.898	19.85	7
092303.53+024739.4	4.669	20.39	7	160501.21–011220.0	4.920	19.78	2
092819.28+534024.2	4.413	19.67	7	161544.13+010401.8*	4.013	20.20	5
095000.17+620318.5	4.062	20.22	6	162048.74+002005.7	4.199	19.36	6
100413.14+630437.3	4.130	20.24	6	211450.34–063257.1	4.268	19.38	7
104837.40–002813.6	4.031	19.05	6	214601.45–075343.6	4.192	19.43	7
105254.59–000625.8	4.173	19.54	6	215817.60–010555.1	4.132	19.73	7
105602.36+003222.0	4.064	19.66	6	221320.00+134832.5	4.129	19.78	7
110819.16–005823.9	4.604	19.87	6	221705.72+135352.7	4.348	20.09	7
112956.10–014212.3	4.850	19.64	7	222050.81+001959.0*	4.700	20.21	6
113745.66+012715.1	4.070	19.72	7	222807.58+003526.2	4.631	19.80	0
115158.23+030341.7	4.701	20.47	7	223521.22–082127.2	4.372	20.07	7
120640.73+033414.9	4.386	19.86	7	224740.17–091511.7	4.174	20.28	7
123115.90–020506.0	4.144	19.75	7	224922.94–010745.8	4.003	19.71	0
123347.21–014853.8	4.259	19.04	7	225246.44+142525.7	4.920	19.91	7
123937.17+674020.7	4.425	20.18	6	230320.38–085433.1	4.337	20.16	7
124757.44–011926.0	4.187	19.83	7	231010.59–100653.9	4.507	20.35	7
125433.56–003922.7	4.291	20.10	6	232112.39+143312.0	4.026	20.24	7
125802.61+022721.2	4.269	19.84	7	233255.72+141916.4	4.751	20.09	7
130039.13+032203.8	4.155	20.09	7	235403.85+155630.3	4.573	20.34	7
130216.13+003032.0	4.607	19.86	6	235718.36+004350.3	4.363	20.13	1
132447.25–031358.2	4.052	19.79	6				

Note. — See Table 1 for an explanation of the columns.